ACS Photonics

Article

pubs.acs.org/journal/apchd5

Ultrahigh Figure-of-Merit in Metal−Insulator−Metal Magnetoplasmonic Sensors Using Low Loss Magneto-optical Oxide Thin Films

Jun Qin,[†,‡] Yan Zhang,[†,‡] Xiao Liang,[†,‡] Chuan Liu,[†,‡] Chuangtang Wang,[†,‡] Tongtong Kang,[†,‡] Haipeng Lu,[†,‡] Li Zhang,[†,‡,§] Peiheng Zhou,[†,‡] Xin Wang,[†,‡] Bo Peng,[†,‡] Juejun Hu,[§] Longjiang Deng,*[,†,‡] and Lei Bi*[,†,‡]

[†]National Engineering Research Center of Electromagnetic Radiation Control Materials and [‡]State Key Laboratory of Electronic Thin-Films and Integrated Devices, University of Electronic Science and Technology of China, Chengdu 610054, China

[§]Department of Materials Science and Engineering, Massachusetts Institute of Technology, Cambridge, Massachusetts 02139, United States

Supporting Information

ABSTRACT: Achieving high figure-of-merit (defined as the ratio between refractive index sensitivity and spectral line width) in surface plasmon sensors is a fundamental quest for ultrasensitive chemical and biomedical sensing applications. Due to ohmic loss of plasmonic metal thin films, the theoretical limit of figure-of-merit is around 54 RIU^{-1} (refractive index unit) for Au-based plasmonic sensors at 650 nm wavelength. Here, we report a way to significantly boost the device figure-of-merit by incorporating low loss magneto-optical oxides in a novel metal−insulator−metal magneto-plasmonic sensor. Our theoretical analysis shows that a record high figure-of-merit of 39600 RIU^{-1} can be achieved in a simple multilayer thin film sensor device at the wavelength of 650 nm, which well exceeds that of conventional surface plasmon resonance sensors at the same wavelength. A high figure-of-merit of 964 ± 150 RIU^{-1} is demonstrated experimentally at 650 nm, 17.8× higher than the theoretical limit of Au surface plasmon resonance sensors at the same wavelength. The high figure-of-merit originates from strong coupling between the magneto-optical waveguide mode and the surface plasmon resonance mode causing a narrow transverse magneto-optical Kerr effect spectrum with Fano line shape at resonant excitation conditions. The limit-of-detection reaches 4.13×10^{-6} RIU, which is 16× higher compared to a standard Au SPR sensor measured on the same setup. Biomedical sensing using bovine serum albumin solutions and biotin−streptavidin interaction demonstrate excellent sensing performance and chemical stability of such metal−insulator−metal magnetoplasmonic sensors.

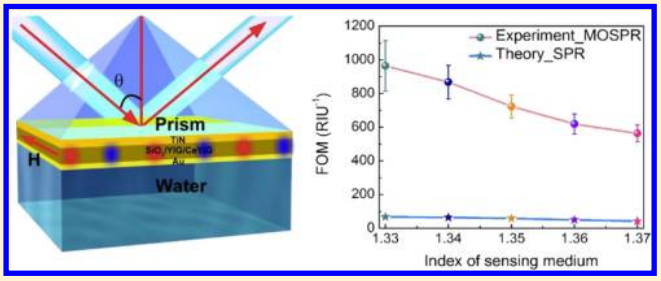

KEYWORDS: *biosensor, magnetoplasmonic, metal−insulator−metal, transverse magneto-optical Kerr effect*

Surface plasmon resonance (SPR) sensors have attracted great research interest recently.[1−12] These devices utilize the collective motion of electrons at the metal-dielectric sensing medium interface, that is, the surface plasmon, whose propagation properties are highly sensitive to the surrounding environment. SPR sensors capitalize on dispersive properties of the SPR mode and tight optical confinement near the sensing surface to claim extraordinarily high surface sensitivity, making it particularly useful for label-free biosensing[3−10,14] and chemical sensing[3,9,10] applications. Its FOM, defined by the device refractive index sensitivity, S, divided by the SPR spectrum full-width at half-maximum (fwhm), Γ, has been widely applied to evaluate the performance of SPR sensors.[8,10,13] Both a high sensitivity, S, and low fwhm can lead to large device FOM. A higher S indicates that spectrum shift is more sensitive to index changes,[15] whereas a lower Γ indicates that the spectrum shift can be more easily discerned for small index changes. Due to the high propagation loss of noble metals, the theoretical limit of FOM in Au based SPR sensors is calculated to be 54 RIU^{-1} at 650 nm wavelength.[16] Significant efforts have been devoted to achieving high FOM SPR sensors in the past decade. The approaches previously explored include nanostructuring the SPR sensor surface,[17] coupling the SPR or LSPR modes to low loss propagating modes,[18,19] introducing signal modulation mechanisms in the sensors,[20,21] and so on. FOMs up to 162 RIU^{-1} have been reported in previous studies.[22,23]

Magneto-optical surface plasmon resonance (MOSPR) sensors have recently been demonstrated to significantly boost the SPR sensor's FOM using the strong magneto-optical effect of magnetic metals such as Fe,[24] Co,[20,25] and Ni.[26] A higher FOM in the transverse magneto-optical Kerr effect

Received: January 29, 2017
Published: May 8, 2017

ACS Publications © 2017 American Chemical Society

DOI: 10.1021/acsphotonics.7b00091
ACS Photonics 2017, 4, 1403−1412

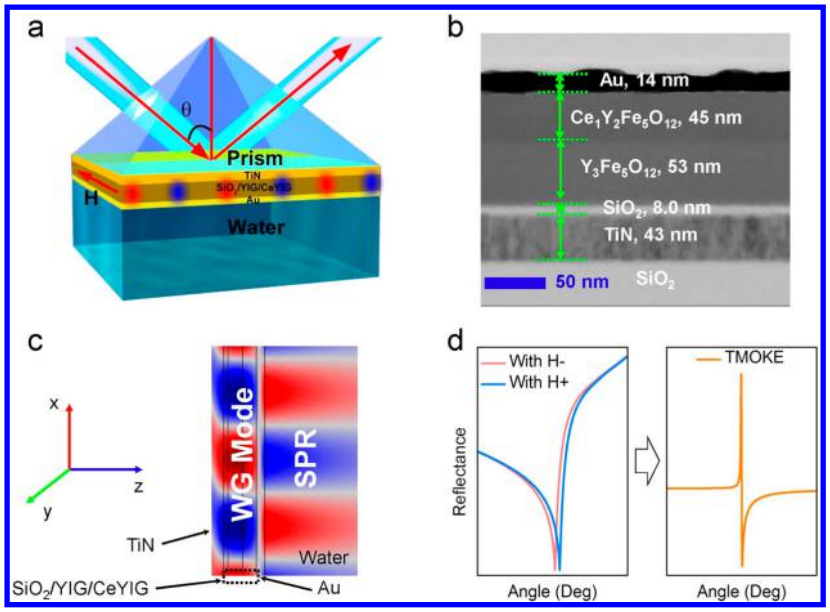

Figure 1. (a) Schematic of the prism coupled MIM MOSPR device. The magnetic field is applied perpendicular to the incident plane. (b) Cross-sectional STEM image of the fabricated device. (c) E_x field profile in the $x-z$ plane when the waveguide (WG) mode hybridizes with the SPR mode. The wavelength of incident light is 650 nm. (d) Typical reflectance and TMOKE spectrum of the device. The hybrid WG-SPR mode features a reflectance spectrum with Fano line shape. The reflectance dip shifts when magnetic fields are applied in opposite directions in the TMOKE configuration, as shown by the red and blue curves, respectively. Typical TMOKE spectrum defined as the difference divided by the sum of the $R(H\pm)$ spectra shows a narrow line width due to the Fano line shape and low optical loss in the magneto-optical oxide thin films, which leads to high device FOM.

(TMOKE) spectrum of MOSPR sensors leads to a sharper spectrum line shape, which also leads to improved LOD compared to SPR sensors.[24,28] In a prism coupled SPR device, instead of monitoring the reflectivity signal of the SPR device, MOSPR sensors measure the transverse magneto-optical Kerr effect (TMOKE) when the SPR mode is excited. The large electromagnetic field concentrated near the magnetic metal films significantly enhances its magneto-optical effect. Subsequently, the propagation constant of the SPR mode is modulated by applying a transverse magnetic field. At a fixed incident angle, this effect leads to different reflectivity of the p-polarized light, that is, the TMOKE effect. Consequently, a narrower line shape of the TMOKE spectrum can be achieved, which enables a much higher FOM, leading to improved SNR and lower LOD of the device compared to conventional SPR devices.[27,28]

Despite the advantages of MOSPR sensors, the high optical loss of magnetic metal film causes significantly broadened resonance spectrum compared to conventional SPR sensors, which compromises the performance improvement.[29−31] MOSPR sensor devices using multilayers of magnetic and noble metal thin films demonstrate FOMs in the range of 20 RIU^{-1} to 191 RIU^{-1} at around 633 nm wavelength.[24,28] Meanwhile, ferromagnetic metals are prone to surface oxidation, which results in deteriorated stability in a liquid environment and limits their application mostly to gas sensing.[32] On the other hand, magneto-optical oxides such as Bi or Ce doped yttrium iron oxides show strong magneto-optical properties and low optical propagation loss in the visible to near-infrared wavelength range.[36−41] The optical loss of noble metals (such as Au) used in SPR sensors is higher than that of the magnetic oxides (see Figure S1). Therefore, one can expect low excess loss when introducing magneto-optical oxides in the SPR devices, and a high FOM MOSPR device can be achieved.

In this paper, we report a novel MOSPR device using low loss magneto-optical oxides, which utilizes the mode coupling effect between a conventional SPR mode and a dielectric magneto-optical metal−insulator−metal (MIM) mode. By properly designing the nonreciprocal phase shift (NRPS) of the MIM waveguide and the coupling strength between the SPR mode and the MIM mode, a record theoretical FOM of 39600 RIU^{-1} is achieved at 650 nm wavelength. A high FOM of 964 ± 150 RIU^{-1} is also demonstrated experimentally at the same wavelength, which is 17.8× higher compared to the theoretical limit of Au SPR sensors at the same wavelength. This MOSPR device can also withstand repeated surface oxygen plasma treatment and is thus highly stable and resistant to oxidation. The high FOM and good chemical stability make these devices very attractive for chemical and biomedical sensing applications. The strategy of coupling SPR modes to a low loss, magneto-optical active dielectric material also opens a new way for developing a variety of MOSPR sensors using low loss magneto-optical oxides.

RESULTS AND DISCUSSION

Figure 1a shows the MIM MOSPR device geometry. The device consists of three layers grown on a double side polished SiO_2 substrate. The bottom metal layer is titanium nitride, a refractory plasmonic material,[35] which can withstand the high temperature processing during deposition of magnetic oxides. The intermediate dielectric layer is a stack comprising (from bottom to top) SiO_2 (8 nm), yttrium iron garnet (YIG; 53 nm), and cerium-substituted yttrium iron garnet (CeYIG) (45 nm) thin films. The 8 nm SiO_2 layer is an amorphous diffusion barrier which prevents TiN from oxidation during high temperature annealing. This amorphous layer also prevents

DOI: 10.1021/acsphotonics.7b00091
ACS Photonics 2017, 4, 1403−1412

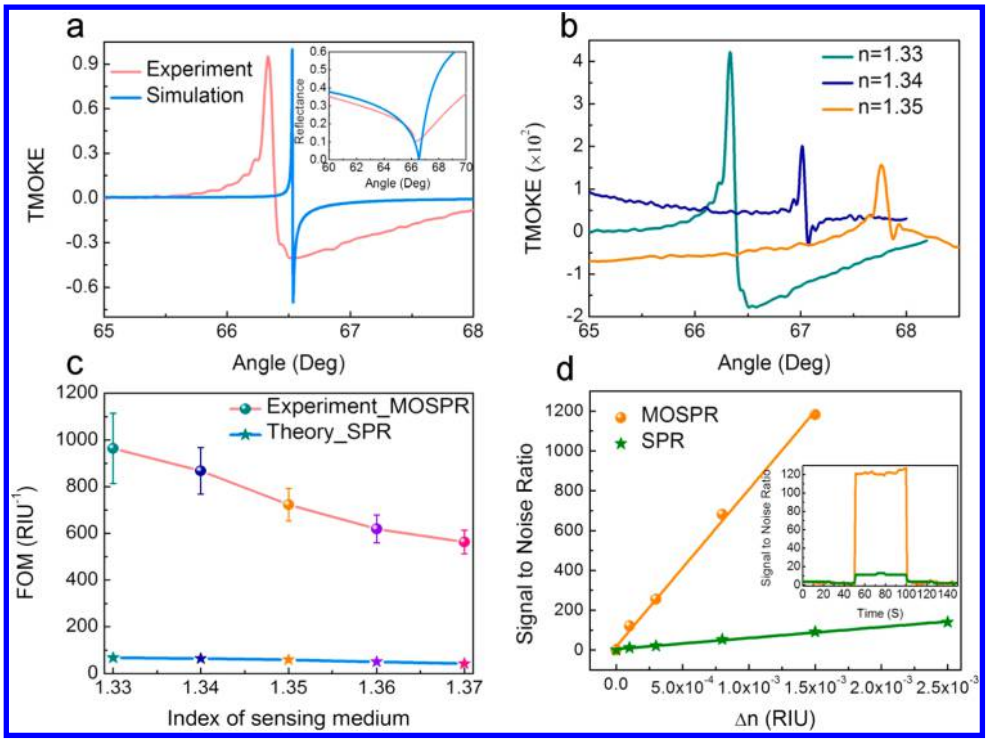

Figure 2. (a) Experimental and simulated normalized TMOKE spectrum as a function of incidence angle. The broader fwhm of the experimental spectrum may be due to the higher loss of gold, CeYIG and TiN than simulations. The inset shows the experiment and simulated reflectance spectrum of the device. The slight difference of the minimum reflectivity angle between experiments and simulations is possibly due to thickness inhomogeneity. (b) TMOKE spectrum as a function of the sensing solution indices. (c) FOM as a function of the sensing solution indices as shown in (c). A maximum FOM of 964 ± 150 RIU^{-1} is obtained for a sensing solution index of 1.33 and incident light wavelength of 650 nm. The error bar is determined from the standard deviation of the measured FOM from five measurements. The simulated maximum theoretical FOM for a traditional Au SPR using SiO_2 (index = 1.45) as the substrate and prism at 650 nm wavelength is also presented. The MIM MOSPR device shows 17.8 times larger FOM than Au SPR sensors when the sensing solution index is 1.33. (d) Measured signal-to-noise ratio as a function of sensing medium index variation for both the MIM MOSPR and SPR devices. The inset shows the real-time SNR variation as changing the sensing medium index by 1×10^{-4}.

templating effect of the TiN crystals to YIG and allows pure magnetic garnet phase crystallization. The YIG layer is a seed layer to promote crystallization of high Ce concentration CeYIG films grown on top. The CeYIG film is the magneto-optical active layer. The topmost Au layer (14 nm) is the SPR mode supporting layer, which also provides a sensing surface with chemical properties identical to those of standard SPR sensors. The trilayer design of SiO_2/YIG/CeYIG also allows strong nonreciprocal phase shift (NRPS) and transverse magneto-optical Kerr (TMOKE) response from the MIM waveguide (see discussions in Figure S4). The cross-sectional scanning tunneling electron microscopy (STEM) image of the fabricated device is shown in Figure 1b. The YIG and CeYIG layers also show crystallized garnet phases and strong magneto-optical Kerr effect at 650 nm wavelength. (See Figure S2a,b) Sharp interfaces between layers are confirmed by EDS mapping, indicating the structural integrity and absence of interdiffusion between the oxide and metal thin films (see Figure S2c).

The device operates under the Kretschmann configuration with a silica prism. Index-matching oil (n = 1.45) is used to attach the SiO_2 substrate to the silica prism. The incident light excites a symmetric propagating waveguide (WG) mode in the MIM structure, as well as an SPR mode at the Au and water interface. When the gold layer is thick, these two modes are independent; whereas when the Au layer is thin enough, these two modes hybridize to form a new WG-SPR mode. The hybrid WG-SPR mode overlaps strongly with both the sensing medium (e.g., water in this case) and the magneto-optical oxide thin films as shown in Figure 1c (see Figure S3). This hybrid mode shows both high sensitivity to the index variation at the water side and strong magneto-optical Kerr effect. The hybrid mode generates a Fano line shape resonance in the reflection spectrum as shown in Figure 1d. When a magnetic field perpendicular to the incident plane is applied across the device, the CeYIG thin film introduces an NRPS of the TM-polarized WG-SPR mode. The reflectance spectrum shifts due to perturbation of mode wave vector by the magneto-optical effect, as shown in Figure 1d, and an enhanced TMOKE is observed. We define TMOKE as[20,39,40]

$$\text{TMOKE} = \frac{R(\text{H}+) - R(\text{H}-)}{R(\text{H}+) + R(\text{H}-)} \quad (1)$$

where $R(\text{H}\pm)$ is the reflectance spectrum under positive and negative applied magnetic fields, respectively. A waveguide enhanced TMOKE spectrum can be obtained from the $R(\text{H}\pm)$ curves, as shown in Figure 1c. Thanks to the Fano line shape of the reflectance spectrum, a strong and narrow TMOKE resonance peak is achieved, which leads to a high device FOM.

To evaluate the bulk index sensitivity, a PDMS microfluidic chip is attached to the sensor surface. Mixtures of deionized water and glycerinum with mass ratios of 0, 7, 15, 22, and 30%, corresponding to refractive indices of 1.33, 1.34, 1.35, 1.36, and 1.37, respectively,[19,26] are injected in the microfluidic chip. The

DOI: 10.1021/acsphotonics.7b00091
ACS Photonics 2017, 4, 1403−1412

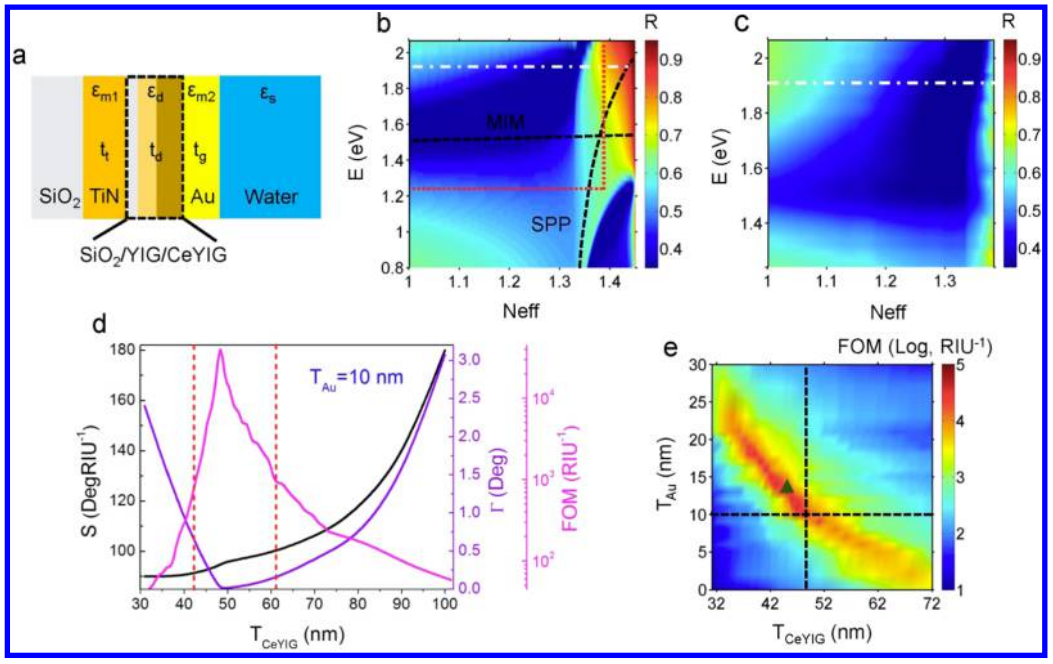

Figure 3. (a) Sketch of the device structure. (b) Simulated dispersion relation of the MIM MOSPR device. The two black dash lines are the uncoupled MIM waveguide mode and SPR mode respectively when the gold layer thickness is t_g = 300 nm. The blue areas indicate the hybrid WG-SPR mode when t_g = 14 nm. (c) Experimentally characterized dispersion relation with t_g = 14 nm for the region within red dash lines shown in (b). The experimental results match well with simulations. (d) Sensitivity S, line width Γ, and FOM as a function of CeYIG layer thickness at the wavelength of 650 nm when Au layer is t_g = 10 nm thick, that is, corresponding to the reflectivity spectrum shown by white dot-dash lines (c) and (d). The vertical red dash lines indicate the borders where FOM values are larger than 10^3 RIU^{-1}. (e) FOM as a function of CeYIG and Au thicknesses. A maximum FOM of 39600 RIU^{-1} is obtained at CeYIG and Au thicknesses of 48 and 10 nm, respectively, indicated by the cross point of the horizontal and vertical dash lines. The dark cyan triangle indicates the experimental device parameters in Figure 2.

reflectance and TMOKE spectrum is characterized using the Kretschmann configuration with a 650 nm wavelength incident light from a laser diode. Figure 2a shows the TMOKE spectrum obtained using eq 1 from both experiments and simulations. For clarity, we normalize both curves. The fwhm of the experimental TMOKE spectrum is 0.09°, fitted using a Fano line shape equation (see Figure S5), which is larger than the simulated value of 0.0074°. This difference is possibly because of the optical loss of our polycrystalline TiN, CeYIG, and Au layers are higher than their single crystal counterparts, whose optical constants were used in simulations.[44,45] The inset of Figure 2a shows the experimental and simulated reflectance spectrum with the sensing medium being pure deionized water. Due to the excitation of a coupled WG-SPR mode, a reflectance spectrum with a Fano resonance dip is observed both from simulation and experiment. The minimum reflectance angles are 66.33° and 66.53° from experiment and simulation, respectively. The measured minimum reflectance is higher than the simulated value, likely due to the large laser beam diameter (~2 mm) used in our experiments. The laser beam samples a large sensor surface area, which is susceptible to slight thin film thickness nonuniformity. Using the perturbation theory, modulation of the SPR wavevector by the applied magnetic field can be expressed as[41−43]

$$\Delta\beta = \frac{\iint \partial_z(\gamma/\varepsilon^2)|H_y(z)|^2 \mathrm{d}z\mathrm{d}y}{\iint \varepsilon^{-1}|H_y|^2 \mathrm{d}z\mathrm{d}y} \tag{2}$$

$$k_0 n \sin\theta = k_{spp}^0 + \Delta\beta \tag{3}$$

where $|H_y(z)|$ is the magnetic field amplitude along the y axis, γ is the off diagonal component of the magneto-optical material's permittivity tensor, ε is the isotropic permittivity (neglecting the off-diagonal components), and k_{spp}^0 is the propagation constant of the SPR-WG mode without external magnetic field. The off-diagonal component of the permittivity tensor of CeYIG ($0.0215i - 0.003$ at 650 nm) induces an NRPS $\Delta\beta$ to the propagation constant of 1.2 rad/mm. From eq 3, this NRPS induces a spectral shift of 10^{-2} degrees theoretically. Experimentally, a spectral shift of $(8 \pm 1) \times 10^{-3}$ degrees is observed. The slightly lower value of angular shift observed by experiments suggests that our CeYIG film may exhibit a weaker magneto-optical effect compared to that of single crystalline CeYIG materials assumed in our theoretical calculations.[33,34] Figure 2b shows the bulk index sensing performance using the TMOKE spectrum with changing the index of solutions from 1.33 to 1.35. The spectrum monotonically shifts to higher angle with increasing solution index due to the larger propagation constant of the WG-SPR hybrid mode. Excellent linearity of the device is observed (see Figure S6a). One also notices that the TMOKE amplitude clearly decreases with increasing solution index. This is because the electromagnetic field shifts to the solution side with its increasing index. The WG-SPR mode is therefore behaving more "SPR-like" with increased attenuation, and the strength of TMOKE signal gradually decreases. The refractive index (RI) sensitivity S, defined as $\mathrm{d}\theta/\mathrm{d}n$, where θ is the resonance angle and n is the index of sensing solutions, is 87.4 degRIU^{-1}. From the fitted fwhm Γ of the TMOKE spectrum (see Figure S5), the FOM, defined as S/Γ, reaches 964 ± 150 RIU^{-1} at 650 nm wavelength in water, as shown in Figure 2c. Large FOMs ranging from 563 ± 50 RIU^{-1} to 964 ± 150 RIU^{-1} are observed in a wide index range of 1.33 to 1.37, suggesting a wide dynamic range for this high FOM index sensor. Five repeated measurements were performed at each

DOI: 10.1021/acsphotonics.7b00091
ACS Photonics 2017, 4, 1403−1412

index value. The error bar mostly comes from the slightly different fwhm's between different measurements. We also put a side-by-side comparison with the FOM of traditional Au SPR sensors at the same wavelength and indices. The MIM MOSPR device shows 17.8× higher FOM compared to SPR devices when the sensing medium has an index of 1.33 (water). The limit of detection (LOD) of both the MOSPR and a standard Au SPR device are characterized by applying an alternating AC magnetic field (500 Oe) at a frequency of 58 Hz perpendicular to the incident plane. The LOD of a standard SPR device with Au (45 nm) on quartz is also measured on the same setup. For both MOSPR and SPR sensing experiments, the real-time detection of the index sensitivity is carried out at the maximum slope for $\Delta R_{pp}/R_{pp}$ or R_{pp} spectrum, respectively.[24] The system noise is defined as the standard deviation of the experimental signal during 50 s with the same index of the sensing medium. The LOD is defined as the index variation where a signal-to-noise ratio (SNR) of 5 is observed by either MOSPR or SPR devices. The measured SNR of the MOSPR and SPR device as a function of the sensing medium index is shown in Figure 2d. The inset shows the real-time SNR variation when changing the solution index by 1×10^{-4}. The measured LOD of the MOSPR and SPR devices are 4.13×10^{-6} and 6.79×10^{-5}, respectively. The MOSPR device shows 16× improvement of the LOD compared to the SPR device, demonstrating the high performance of the MOSPR device.

To elucidate the origin of such high FOMs in the MIM MOSPR device, we simulated and experimentally characterized the dispersion relation of the SPR-WG mode. The simulated device structure is shown in Figure 3a. The bottom TiN metal layer with permittivity ε_{m1} has a finite thickness of t_t. The intermediate SiO_2/YIG/CeYIG thin film stack can be generalized as a dielectric layer with an effective permittivity of ε_d and a thickness of t_d. The top Au layer has a permittivity of ε_{m2} and a thickness of t_g, and the semi-infinite sensing medium has a uniform permittivity of ε_s. When t_g is sufficiently large, the system can be treated as two separate subsystems. On the left side of Au is an MIM waveguide. Two SPR modes at the Au/dielectric and TiN/dielectric interfaces hybridize, resulting in a symmetric WG mode and an antisymmetric WG mode, characterized by symmetric and antisymmetric distributions of their tangential electric fields.[46] On the right side of t_g is an SPR waveguide. The SPR mode is supported by the interface between Au and water. Hybridization between the WG and SPR mode occurs when these two subsystems are brought into close proximity with a small Au metal film thickness t_g. The simulation and characterization below illustrate how the modes hybridize by fixing the device geometries and investigating the dispersion relation when t_g is as thin as 14 nm. Meanwhile, the CeYIG layer thickness t_c and Au layer thickness t_g are also optimized for the best FOM.

The dispersion relation is simulated using the 4 × 4 transfer matrix method which takes account of the permittivity tensor of anisotropic magneto-optical materials.[47] For dispersion relation simulations, the device geometry is the same as what we used in the experiments shown in Figure 1b (TiN 43 nm/SiO_2 8 nm/YIG 53 nm/CeYIG 45 nm/Au 14 nm). The permittivity of TiN and Au are defined by the Drude-Lorentz model[44] and the Drude model,[45] respectively. The sensing medium is chosen as water (ε_s = 1.769). The permittivity tensor of the YIG and CeYIG layers at 650 nm wavelength are obtained from refs 48 and 49, with the diagonal and off diagonal components chosen as $\varepsilon_{dia} = 5.85 + i0.133$ and $\varepsilon_{off} = i0.0215 - 0.003$ for CeYIG, and $\varepsilon_{dia} = 4.93 + i0.0177$ and $\varepsilon_{off} = i0.00049$ for YIG, respectively. The SiO_2 index is 1.45. The black dash curves in the contour map of Figure 3b outlines the dispersion relations of the MIM mode and SPR mode respectively when they are decoupled, that is, the metal thickness t_g is thick enough (200 nm). The crossing point is at a photon energy of 1.5 eV with mode effective index 1.38. For a SiO_2 prism with index of 1.45 used in this study, it possible to excite these two modes simultaneously. The contour map of Figure 3b shows the reflectance as a function of photon energy and mode effective index with t_g = 14 nm. The two modes hybridize with each other, leading to an anticross line shape resembling Rabbi-like splitting,[50−52] as shown by the blue colored low reflectivity regions. To confirm the theoretical results, we measured the dispersion relation of our device by performing angular reflectance scans with different incident wavelengths from a supercontinuum laser source. The wavelength and angle of our characterizations covered the red box region in Figure 3b. As shown in Figure 3c, the experiment results are consistent with the simulations. The white dash-dot line in both Figure 3b and c indicates where our sensing experiments are performed, that is, the reflectance spectrum shown in Figure 2a. Therefore, both simulation and experiments confirmed hybridization of the WG and SPR modes.

We now turn to the influence of device geometries on the FOM. The Au layer thickness t_g and CeYIG thickness t_c are the main factors influencing the mode hybridization and magneto-optical effect of the device. We first fix t_g as 10 nm and vary the CeYIG layer thickness. Figure 3d shows the evolution of the sensitivity S, the fwhm of the TMOKE spectrum Γ and the FOM as a function of the CeYIG layer thickness. When CeYIG is thin (<50 nm), the mode is mostly localized between the TiN and the Au layers, that is, more WG mode-like. S is relatively low in this case due to less interaction of the mode with water. Γ is also large due to the strong interaction of the mode with the TiN layer with higher loss. When CeYIG is thick (>50 nm), the mode is more localized on the water side, that is, more SPR mode-like. The stronger mode overlap with the sensing medium leads to higher S. Notice that S can reach 180 degRIU^{-1} or higher when CeYIG is sufficiently thick, which exceeds the conventional Au SPR sensor at this wavelength. This has been reported in previous studies.[53] When the dielectric layer in the MIM structure is several hundred nanometers thick, the sensitivity can be enhanced by more than 50% concurrent with a narrow line width.[53] Interestingly, when the CeYIG layer thickness is intermediate, the WG-SPR mode resonantly couples to the incident light with low reflectivity. A very narrow TMOKE spectrum can be achieved that leads to high FOM. This narrow TMOKE spectrum is first due to a strong mode overlap with the MIM magneto-optical waveguide, which leads to strong TMOKE effect and large $R(+H)-R(-H)$ values in eq 1, and second due to the optimum CeYIG thickness, conducive to low reflectance of the device. This optimum CeYIG layer thickness resembles an optimum Au layer thickness in SPR devices, where lowest reflectivity and maximum field enhancement is achieved at the metal/sensing medium interface.[54] It should be noted that high FOM can be achieved with a large fabrication window. Considering the fabrication tolerance, for a CeYIG thickness range of 42 to 63 nm, the FOM can be above 10^3 RIU^{-1}. The discussion above can be extended to a parameter space constructed by the thickness of Au (t_g) and CeYIG (t_c), as shown in Figure 3e. A bright high FOM region is achieved where the Au and CeYIG

DOI: 10.1021/acsphotonics.7b00091
ACS Photonics 2017, 4, 1403−1412

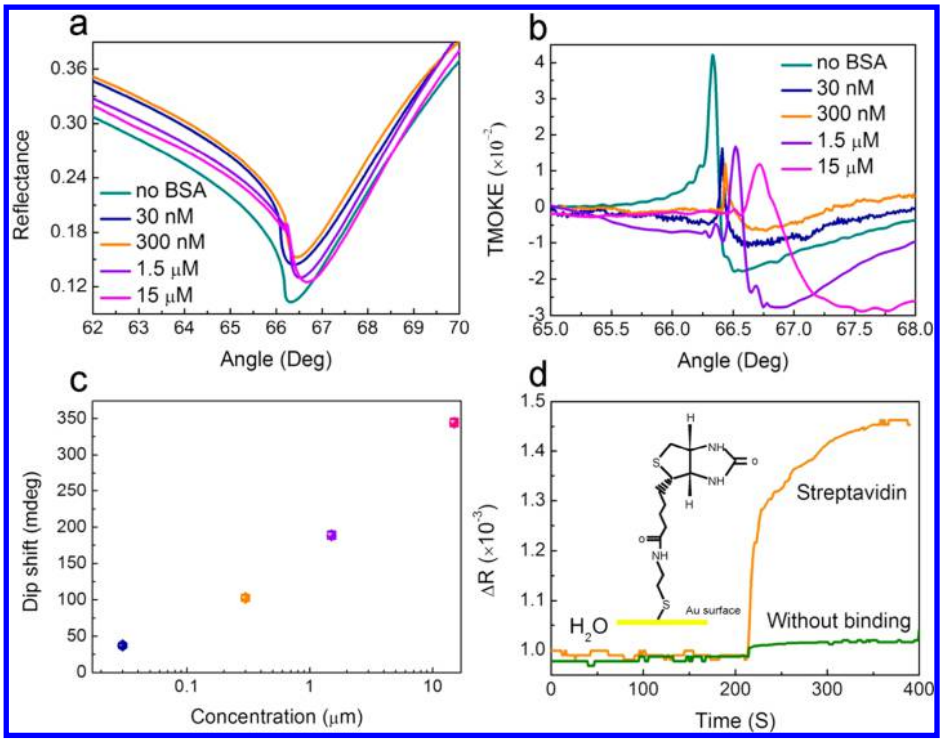

Figure 4. (a) Reflectance spectra of the MIM sensor for sensing different BSA solution concentrations, ranging from 15 μM to 30 nM. The BSA solution was drop-casted on the sensor surface and dried at room temperature. The spectrum of the sample without BSA was provided as a reference. (b) TMOKE spectra of the sensing experiments shown in (a). (c) Resonance dip shift of the MOKE spectrum as a function of BSA concentration. The error bar is the experimental error in the reflectance angle spectrum for five consecutive measurements. (d) Temporal response of the MOSPR signal for the streptavidin binding process on a biotin modified MIM MOSPR sensor.

thickness are optimum to yield large TMOKE signals. On the top right region, the mode is more SPR-like with higher S, larger Γ, and lower FOM, and on the bottom left region, the mode is more WG-like with lower S, larger Γ and lower FOM. The highest FOM from this plot is 39600 RIU^{-1} with t_g = 10 nm and t_c = 48 nm, respectively, indicated by the cross point of the horizontal and vertical dash lines. The experimentally realized sensor structure in Figure 2 is indicated in Figure 3e by a dark cyan triangle, showing a little deviation from the optimal point. The theoretical FOM of this device from Figure 3e is 13288 RIU^{-1}. The lower FOM values observed in experiments are predominately due to the wider Γ in the reflectance spectrum and TMOKE spectrum, as discussed in Figure 2a,b. Therefore, this device has a significant potential to obtain better FOM with improved thickness control and optical loss optimization.

The Au surface of the MIM MOSPR senor creates a surface chemistry identical to that of conventional SPR sensors. To demonstrate the capability of using our device as a plasmonic biosensor, the MIM MOSPR device was applied to biosensing experiments using Bovine Serum Albumin (BSA) with a molecular weight of 66776 Da as a model molecule. A 15 μM BSA solution was first prepared by dissolving BSA powders in distilled water. The solution was then serial diluted to a series of concentrations down to 30 nM. The BSA solution was then drop-casted on the gold surface followed by ambient drying at room temperature. Therefore, the protein molecules were nonspecifically bound to the gold surface.[10,55,56] Subsequently, the sensor chip was loaded on a prism coupling system with the microfluidic chip attached on the sensor surface. The MOSPR sensing spectrum was collected with distilled water injected into the microfluidic chip. Thus, the BSA molecules are bonded only to the very surfaces of the sensor with a fixed index of 1.33 within the bulk of the sensing medium. After sensing test each time, the sensor surface was regenerated by rinsing in deionized water and O_2 plasma cleaning at 55 W for 60 s. The reflectance spectrum consistently returns to the original state, indicating stability of our device against oxidation environments (see Figure S6b). Figure 4a,b shows a series of reflectance spectra and TMOKE spectrum of the sensor device when it is exposed to different BSA concentrations. For both types of spectra, the resonance dip shifts to higher angles with increasing the BSA concentrations. However, the FOM is vastly different. The TMOKE spectrum shows much narrower line shape compared to the reflectance spectrum. One can also see that the TMOKE spectrum broadens as the BSA concentration increases. This is due to the higher index BSA molecules adsorbed on the Au surface driving the mode toward the water side. The structure deviates from the ideal coupling condition and the device FOM decreases. The BSA molecules at the Au film surface may also introduce more scattering loss to broaden the TMOKE spectrum. The concentration dependence of the peak position is extracted and plotted in Figure 4c. The error bar is then determined by the standard deviation of the peak shift for five consecutive experimental measurements. The small error bar indicates the reliability of the sensing results. The sensitivity of the MIM MOSPR device reaches 23 mdeg/μM. The experiment demonstrates the capability of biosensing using our MIM MOSPR sensors down to the nM concentration range. To evaluate the analyte binding process to our sensor surface, we monitored the MOSPR signal during the dynamic binding process of streptavidin to biotin on the sensor device, which is widely used to evaluate biosensing process on SPR devices.[57] The sensor surface is first modified by biotin, then

DOI: 10.1021/acsphotonics.7b00091
ACS Photonics 2017, 4, 1403−1412

the real-time MOSPR signal is monitored by flowing a 0.05 g/L streptavidin solution as shown in Figure 4d (see Methods). The MOSPR signal ΔR for a pristine sensor device without biotin modification is also shown for comparison. The changing of ΔR is much larger on the biotin modified sensor surface than the pristine surface, therefore, demonstrating the binding process of biotin and streptavidin and the excellent biosensing performance of the MOSPR device.

By applying low loss magneto-optical garnet thin films, we demonstrate a novel MIM MOSPR sensing device in this paper. The MIM MOSPR device features several advantages. First, the low loss magnetic oxide thin films relax the loss considerations in device design. In metallic magnetic metal-based MOSPR sensors, a fundamental trade-off is between the magnetic metal loss and its magneto-optical properties. In MIM MOSPR devices using low loss CeYIG, this trade-off relaxes to finding both an optimum thickness for mode excitation and strongest magneto-optical effect. As shown in Figure 3e, this relaxed design criteria leads to a wide range of Au-CeYIG thickness combinations with large FOMs, which eases experimental fabrication. Second, the oxide nature of all the dielectric layers guarantees superior chemical stability (in particular, against oxidation). As demonstrated in the biosensing experiment, the device can be reused many times after oxygen plasma treatment of the surface. Third, the Fano resonance observed in the WG-SPR coupled mode is unique for this type of devices. The asymmetric Fano line shape reflectance spectrum in turn boosts the observed TMOKE. Optimizing this Fano resonance with different metal and dielectric materials or wavelengths may further improve the device performance.[58] The incorporation of low loss magnetic oxides in plasmonic sensing devices may also trigger the development of a variety of novel device structures in the future. One may notice that the device demonstrated in this study uses a very simple multilayer thin film structure. Although 1D[27] or 2D[20] photonic crystal structures have been proposed or demonstrated to show narrow spectral features. Compared to the photonic crystal structures,[27] our MIM device shows higher index sensitivity due to a higher modal overlap with the sensing medium as well as less complexity of device fabrication. The MIM structure using magnetic oxides can also be used in localized SPR (LSPR) devices.[59,60] Moreover, such devices can also be used in gas sensing. We also theoretically demonstrated a high FOM of 595 RIU^{-1} when the sensing medium is air, using the same sensing device presented in this paper (see Figure S7). All these possibilities indicate that MIM MOSPR devices using low loss magnetic oxides are promising candidates for high performance chemical and biomedical sensing applications.

CONCLUSIONS

In summary, we have designed and fabricated a MIM MOSPR sensor using low loss magneto-optical CeYIG thin films. The device is composed of a TiN bottom metal layer, CeYIG with dielectric buffer middle layers and a top gold metal sensing layer. A strong WG-SPR coupled mode is excited by prism coupling in the Kretchmann configuration, which leads to a Fano line shape resonance. The TMOKE spectrum due to the nonreciprocal phase shift of the WG mode show sharp resonances at proper CeYIG and Au layer thicknesses, which leads to a high device FOM of 39600 RIU^{-1} numerically and 964 ± 150 RIU^{-1} experimentally. Biosensing experiments using BSA show high FOM of the device in a wide concentration range of 30 nM to 15 μM. Our study opens up high performance plasmonic chemical and biomedical sensing applications based on using low loss magneto-optical oxides.

METHODS

Sensor Fabrication. The sensor thin film stack of 43 nm TiN/8 nm SiO_2/53 nm YIG/45 nm CeYIG/2 nm Ti/14 nm Au was deposited on double side polished silica substrates using pulsed laser deposition (PLD), sputtering, and thermal evaporation. The bottom TiN was first deposited by PLD (TSST, Netherlands) equipped with a 248 nm KrF excimer laser in 0.5 Pa nitrogen ambient at 800 °C. The base pressure was 1×10^{-6} Pa. The laser fluence was 3 J/cm^2. After deposition, the sample was cooled down in flowing nitrogen at a rate of 5 °C/min to room temperature. Then the sample was transferred to a sputtering chamber with base pressure of 1×10^{-4} Pa. A thin layer of SiO_2 was sputtered onto the TiN film to prevent TiN oxidation and promote YIG and CeYIG crystallization. A 53 nm thick YIG thin film was deposited on the SiO_2 layer at room temperature by PLD and rapid thermal annealed in N_2 atmosphere at 860 °C for 3 min. After YIG film crystallization, the CeYIG film was also deposited at room temperature and rapid thermal annealed in N_2 at 800 °C for 3 min. Finally, 2 nm Ti and 14 nm Au were thermally evaporated at room temperature as the top layer.

Sensing Experiments Using a Prism Coupling System. The reflectance and TMOKE spectrum of waveguide coupled MOSPR was measured by the attenuated total reflection method using the Kretschmann configuration as shown in Figure 1a. The SiO_2 substrate was attached to a silica prism (n = 1.45) using index-matching oil (Cargille, n = 1.45). A PDMS microfluidic chip was attached to the surface of the sensor for solution sensing evaluation. Angle-resolved reflection spectra of the device were measured on a θ–2θ rotation table driven by a microprocessor-controlled stepping motor (with a resolution of 0.001°). A semiconductor monochromatic laser source (λ = 650 nm) was incident onto the sample interface through a linear polarizer to maintain a p-polarization. A beam splitter was placed between the polarizer and sample to split the incident light to a reference detector for incident angle calibration. The reflected light from the sensor was detected by a Si photodiode. The dispersion relation of the sensor was characterized using a supercontinuum laser (NKT Photonics) and the θ–2θ rotation table in a wavelength range of 600 to 1000 nm. The reflection spectrum of the sensor device as a function of incident angle was collected at 5 nm wavelength intervals. The dispersion relation is then plotted as the photon energy versus effective index following the relationship of $E = \hbar\omega$ and $N_{eff} = N_{prism} \sin \theta_0$, where θ_0 is the resonant angle.

Absorption Biosensing Experiments. BSA solutions were prepared by dissolving 0.01 g BSA powders to 10 mL of deionized water and followed by serial dilution to form solutions with concentrations from 30 nM to 15 μM. The BSA solution was then drop-casted on the sensor gold film surface and dried at room temperature leading to nonspecifically binding of BSA molecules to the sensor surface. Reflectance spectra were taken afterward using the prism coupling system with water covering the sensor surface. After each measurement, the same chip was soaked in the deionized water and cleaned by ultrasonication, plus O_2 plasma surface cleaning at 55 W for 60 s. The reflection spectrum of the sensor after cleaning was verified to be identical to that before BSA binding.

Biotin–Streptavidin Bonding Biosensing Experiments. The device surface was first cleaned in O_2 plasma

DOI: 10.1021/acsphotonics.7b00091
ACS Photonics 2017, 4, 1403–1412

(60 W 1 min), followed by ultrasonicating in ethanol and deionized water for 20 min, respectively. Then the sample was immersed in 10 mM 2-aminoethanethiol solution in ethanol for 24 h. After incubation, the excess 2-aminoethanethiol was rinsed off with ethanol and deionized water. The sample was then soaked in a 5 mM saturated (+)-biotin *N*-hydroxysuccinimide ester solution in phosphate-buffered saline (PBS, PH 7.2) for 4 h. Finally, the sample was transferred into 1 mg/mL Bovine serum albumin (BSA) solution in deionized water to block unoccupied sites and prevent nonspecific binding to the sensor surface. The suspension bond of biotin to the sensor surface is formed by these processes. For detecting the binding process of streptavidin with biotin, we dilute 0.05 g/L streptavidin solution in deionized water. The real-time MOSPR signal is collected by first inject water, then streptavidin solution to the device surface with a microfluidic chip. All chemicals are purchased from Sigma.

■ ASSOCIATED CONTENT

Supporting Information

The Supporting Information is available free of charge on the ACS Publications website at DOI: 10.1021/acsphotonics.7b00091.

Optical loss and figure of merit of CeYIG films compared to those of Au and ferromagnetic metals (Figure S1), material and device structure characterizations (Figure S2), mode evolution with changing Au thickness (Figure S3), nonreciprocal phase shift (NRPS) and absorption loss of the MIM waveguide (Figure S4), fitting of the transverse magneto-optical kerr effect (TMOKE) spectrum by a Fano line shape (Figure S5), linearity and stability of the sensor device (Figure S6), and gas sensing performance with the sensing medium being air (Figure S7; PDF).

■ AUTHOR INFORMATION

Corresponding Authors

*E-mail: denglj@uestc.edu.cn.
*E-mail: bilei@uestc.edu.cn.

ORCID

Bo Peng: 0000-0001-9411-716X
Lei Bi: 0000-0002-2698-2829

Notes

The authors declare no competing financial interest.

■ ACKNOWLEDGMENTS

The authors are grateful for the assistance of Ti and Au evaporation by Prof. Chun Li. This project is supported by the National Natural Science Foundation of China (61475031, 51522204), Ministry of Science and Technology of China MOST No. 2016YFA0300802, the Fundamental Research Funds for the Central Universities (ZYGX2014Z001), the Science Foundation for Youths of Sichuan Province (2015JQO014), and the U.S. National Science Foundation Award #1607865.

■ REFERENCES

(1) Barnes, W. L.; Dereux, A.; Ebbesen, T. W. Surface Plasmon Subwavelength Optics. *Nature* **2003**, *424*, 824−830.

(2) Uchida, K.; Adachi, H.; Kikuchi, D.; Ito, S.; Qiu, Z.; Maekawa, S.; Saitoh, E. Generation of Spin Currents by Surface Plasmon Resonance. *Nat. Commun.* **2015**, *6*, 5910.

(3) Zeng, S.; Baillargeat, D.; Ho, H. P.; Yong, K. T. Nanomaterials Enhanced Surface Plasmon Resonance for Biological and Chemical Sensing Applications. *Chem. Soc. Rev.* **2014**, *43*, 3426−3452.

(4) Zijlstra, P.; Paulo, P. M.; Orrit, M. Optical Detection of Single Non-absorbing Molecules Using the Surface Plasmon Resonance of a Gold Nanorod. *Nat. Nanotechnol.* **2012**, *7*, 379−382.

(5) Ouyang, Q.; Zeng, S.; Jiang, L.; Hong, L.; Xu, G.; Dinh, X. Q.; Qian, J.; He, S.; Qu, J.; Coquet, P.; Yong, K. T. Sensitivity Enhancement of Transition Metal Dichalcogenides/Silicon Nanostructure-based Surface Plasmon Resonance Biosensor. *Sci. Rep.* **2016**, *6*, 28190.

(6) Kravets, V. G.; Schedin, F.; Jalil, R.; Britnell, L.; Gorbachev, R. V.; Ansell, D.; Thackray, B.; Novoselov, K. S.; Geim, A. K.; Kabashin, A. V.; Grigorenko, A. N. Singular Phase Nano-optics in Plasmonic Metamaterials for Label-free Single-molecule Detection. *Nat. Mater.* **2013**, *12*, 304−309.

(7) Im, H.; Shao, H.; Park, Y. I.; Peterson, V. M.; Castro, C. M.; Weissleder, R.; Lee, H. Label-free Detection and Molecular Profiling of Exosomes with a Nano-plasmonic Sensor. *Nat. Biotechnol.* **2014**, *32*, 490.

(8) Shen, Y.; Zhou, J.; Liu, T.; Tao, Y.; Jiang, R.; Liu, M.; Xiao, G.; Zhu, J.; Zhou, Z. K.; Wang, X.; Jin, C.; Wang, J. Plasmonic Gold Mushroom Arrays with Refractive Index Sensing Figures of Merit Approaching the Theoretical Limit. *Nat. Commun.* **2013**, *4*, 2381.

(9) Shrivas, K.; Shankar, R.; Dewangan, K. Gold Nanoparticles as a Localized Surface Plasmon Resonance Based Chemical Sensor for On-site Colorimetric Detection of Arsenic in Water Samples. *Sens. Actuators, B* **2015**, *220*, 1376−1383.

(10) Xu, X.; Peng, B.; Li, D.; Zhang, J.; Wong, L. M.; Zhang, Q.; Wang, S.; Xiong, Q. Flexible Visible−infrared Metamaterials and Their Applications in Highly Sensitive Chemical and Biological Sensing. *Nano Lett.* **2011**, *11*, 3232−3238.

(11) Piliarik, M.; Homola, J. Surface Plasmon Resonance (SPR) Sensors: Approaching Their Limits? *Opt. Express* **2009**, *17*, 16505−16517.

(12) Homola, J.; Yee, S. S.; Gauglitz, G. Surface Plasmon Resonance Sensors: Review. *Sens. Actuators, B* **1999**, *54*, 3−15.

(13) Estevez, M. C.; Otte, M. A.; Sepulveda, B.; Lechuga, L. M. Trends and Challenges of Refractometric Nanoplasmonic Biosensors: A Review. *Anal. Chim. Acta* **2014**, *806*, 55−73.

(14) Homola, J.; Koudela, I.; Yee, S. S. Surface Plasmon Resonance Sensors Based on Diffraction Gratings and Prism Couplers: Sensitivity Comparison. *Sens. Actuators, B* **1999**, *54*, 16−24.

(15) Justino, C. I.; Rocha-Santos, T. A.; Duarte, A. C. Review of Analytical Figures of Merit of Sensors and Biosensors in Clinical Applications. *TrAC, Trends Anal. Chem.* **2010**, *29*, 1172−1183.

(16) Huang, D. W.; Ma, Y. F.; Sung, M. J.; Huang, C. P. Approach the Angular Sensitivity Limit in Surface Plasmon Resonance Sensors with Low Index Prism and Large Resonant Angle. *Opt. Eng.* **2010**, *49*, 054403−054403.

(17) Zeng, B.; Gao, Y.; Bartoli, F. J. Rapid and Highly Sensitive Detection Using Fano Resonances in Ultrathin Plasmonic Nanogratings. *Appl. Phys. Lett.* **2014**, *105*, 161106.

(18) Liu, Y.; Kim, J. Numerical Investigation of Finite Thickness Metal-Insulator-Metal Structure for Waveguide-based Surface Plasmon Resonance Biosensing. *Sens. Actuators, B* **2010**, *148*, 23−28.

(19) Lee, K. S.; Son, J. M.; Jeong, D. Y.; Lee, T. S.; Kim, W. M. Resolution Enhancement in Surface Plasmon Resonance Sensor Based on Waveguide Coupled Mode by Combining a Bimetallic Approach. *Sensors* **2010**, *10*, 11390−11399.

(20) Caballero, B.; García-Martín, A.; Cuevas, J. C. Hybrid Magnetoplasmonic Crystals Boost the Performance of Nanohole Arrays as Plasmonic Sensors. *ACS Photonics* **2016**, *3*, 203−208.

(21) Wen, K.; Hu, Y.; Chen, L.; Zhou, J.; Lei, L.; Guo, Z. Fano Resonance with Ultra-high Figure of Merits Based on Plasmonic Metal-Insulator-Metal Waveguide. *Plasmonics* **2015**, *10*, 27−32.

(22) Vala, M.; Chadt, K.; Piliarik, M.; Homola, J. High-performance Compact SPR Sensor for Multi-analyte Sensing. *Sens. Actuators, B* **2010**, *148*, 544−549.

DOI: 10.1021/acsphotonics.7b00091
ACS Photonics 2017, 4, 1403−1412

(23) Yanik, A. A.; Cetin, A. E.; Huang, M.; Artar, A.; Mousavi, S. H.; Khanikaev, A.; Connor, J. H.; Shvets, G.; Altug, H. Seeing Protein Monolayers with Naked Eye Through Plasmonic Fano Resonances. *Proc. Natl. Acad. Sci. U. S. A.* **2011**, *108*, 11784−11789.
(24) Regatos, D.; Fariña, D.; Calle, A.; Cebollada, A.; Sepúlveda, B.; Armelles, G.; Lechuga, L. M. Au/Fe/Au Multilayer Transducers for Magneto-optic Surface Plasmon Resonance Sensing. *J. Appl. Phys.* **2010**, *108*, 054502.
(25) Regatos, D.; Sepúlveda, B.; Fariña, D.; Carrascosa, L. G.; Lechuga, L. M. Suitable Combination of Noble/Ferromagnetic Metal Multilayers for Enhanced Magneto-plasmonic Biosensing. *Opt. Express* **2011**, *19*, 8336−8346.
(26) Maccaferri, N.; Gregorczyk, K. E.; de Oliveira, T. V.; Kataja, M.; van Dijken, S.; Pirzadeh, Z.; Dmitriev, A.; Akerman, J.; Knez, M.; Vavassori, P. Ultrasensitive and Label-free Molecular-level Detection Enabled by Light Phase Control in Magnetoplasmonic Nanoantennas. *Nat. Commun.* **2015**, *6*, 6150.
(27) Ignatyeva, D. O.; Knyazev, G. A.; Kapralov, P. O.; Dietler, G.; Sekatskii, S. K.; Belotelov, V. I. Magneto-optical Plasmonic Heterostructure with Ultranarrow Resonance for Sensing Applications. *Sci. Rep.* **2016**, *6*, 28077.
(28) Sepúlveda, B.; Calle, A.; Lechuga, L. M.; Armelles, G. Highly Sensitive Detection of Biomolecules with the Magneto-optic Surface-Plasmon-Resonance Sensor. *Opt. Lett.* **2006**, *31*, 1085−1087.
(29) Armelles, G.; Cebollada, A.; García-Martín, A.; González, M. U. Magnetoplasmonics: Combining Magnetic and Plasmonic Functionalities. *Adv. Opt. Mater.* **2013**, *1*, 10−35.
(30) Armelles, G.; Cebollada, A.; García-Martín, A.; García-Martín, J. M.; González, M. U.; González-Díaz, J. B.; Ferreiro-Vila, E.; Torrado, J. F. Magnetoplasmonic Nanostructures: Systems Supporting Both Plasmonic and Magnetic Properties. *J. Opt. A: Pure Appl. Opt.* **2009**, *11*, 114023.
(31) Banthí, J. C.; Meneses-Rodríguez, D.; García, F.; González, M. U.; García-Martín, A.; Cebollada, A.; Armelles, G. High Magneto-optical Activity and Low Optical Losses in Metal-Dielectric Au/Co/Au-SiO_2 Magnetoplasmonic Nanodisks. *Adv. Mater.* **2012**, *24*, OP36−OP41.
(32) González-Díaz, J. B.; García-Martín, A.; García-Martín, J. M.; Cebollada, A.; Armelles, G.; Sepúlveda, B.; Alaverdyan, Y.; Käll, M. Plasmonic Au/Co/Au Nanosandwiches with Enhanced Magneto-optical Activity. *Small* **2008**, *4*, 202−205.
(33) Bi, L.; Hu, J.; Jiang, P.; Kim, H. S.; Kim, D. H.; Onbasli, M. C.; Dionne, G. F.; Ross, C. A. Magneto-optical Thin Films for On-chip Monolithic Integration of Non-reciprocal Photonic Devices. *Materials* **2013**, *6*, 5094−5117.
(34) Zhang, Y.; Xie, J.; Deng, L.; Bi, L. Growth of Phase Pure Yttrium Iron Garnet Thin Films on Silicon: the Effect of Substrate and Postdeposition Annealing Temperatures. *IEEE Trans. Magn.* **2015**, *51*, 1−4.
(35) Kehlberger, A.; Richter, K.; Onbasli, M. C.; Jakob, G.; Kim, D. H.; Goto, T.; Ross, C. A.; Gotz, G.; Reiss, G.; Kuschel, T.; Kläui, M. Enhanced Magneto-optic Kerr Effect and Magnetic Properties of $CeY_2Fe_5O_{12}$ Epitaxial Thin Films. *Phys. Rev. Appl.* **2015**, *4*, 014008.
(36) Onbasli, M. C.; Beran, L.; Zahradník, M.; Kučera, M.; Antoš, R.; Mistrík, J.; Dionne, G. F.; Veis, M.; Ross, C. A. Optical and Magneto-optical Behavior of Cerium Yttrium Iron Garnet Thin Films at Wavelengths of 200−1770 nm. *Sci. Rep.* **2016**, *6*, 23640.
(37) Hansen, P.; Krumme, J. P. Magnetic and Magneto-optical Properties of Garnet Films. *Thin Solid Films* **1984**, *114*, 69−107.
(38) Naik, G. V.; Schroeder, J. L.; Ni, X.; Kildishev, A. V.; Sands, T. D.; Boltasseva, A. Titanium Nitride as a Plasmonic Material for Visible and Near-infrared Wavelengths. *Opt. Mater. Express* **2012**, *2*, 478−489.
(39) Ferreiro-Vila, E.; García-Martín, J. M.; Cebollada, A.; Armelles, G.; González, M. U. Magnetic Modulation of Surface Plasmon Modes in Magnetoplasmonic Metal-Insulator-Metal Cavities. *Opt. Express* **2013**, *21*, 4917−4930.
(40) Ferreiro-Vila, E.; González-Díaz, J. B.; Fermento, R.; González, M. U.; García-Martín, A.; García-Martín, J. M.; Cebollada, A.; Armelles, G.; Meneses-Rodriguez, D.; Sandoval, E. M. Intertwined Magneto-optical and Plasmonic Effects in Ag/Co/Ag Layered Structures. *Phys. Rev. B: Condens. Matter Mater. Phys.* **2009**, *80*, 125132.
(41) Bi, L.; Hu, J.; Jiang, P.; Kim, D. H.; Dionne, G. F.; Kimerling, L. C.; Ross, C. A. On-chip Optical Isolation in Monolithically Integrated Non-reciprocal Optical Resonators. *Nat. Photonics* **2011**, *5*, 758−762.
(42) Espinola, R. L.; Izuhara, T.; Tsai, M. C.; Osgood, R. M.; Dötsch, H. Magneto-optical Nonreciprocal Phase Shift in Garnet/Silicon-on-Insulator Waveguides. *Opt. Lett.* **2004**, *29*, 941−943.
(43) Roh, S.; Chung, T.; Lee, B. Overview of the Characteristics of Micro- and Nano-structured Surface Plasmon Resonance Sensors. *Sensors* **2011**, *11*, 1565−1588.
(44) Chen, N. C.; Lien, W. C.; Liu, C. R.; Huang, Y. L.; Lin, Y. R.; Chou, C.; Chang, S. Y.; Ho, C. W. Excitation of Surface Plasma Wave at TiN/Air Interface in the Kretschmann Geometry. *J. Appl. Phys.* **2011**, *109*, 043104−043104−7.
(45) Ordal, M. A.; Long, L. L.; Bell, R. J.; Bell, S. E.; Bell, R. R.; Alexander, R. W.; Ward, C. A. Optical Properties of the Metals Al, Co, Cu, Au, Fe, Pb, Ni, Pd, Pt, Ag, Ti, and W in the Infrared and Far Infrared. *Appl. Opt.* **1983**, *22*, 1099−1119.
(46) Dionne, J. A.; Sweatlock, L. A.; Atwater, H. A.; Polman, A. Plasmon Slot Waveguides: Towards Chip-scale Propagation with Subwavelength-scale Localization. *Phys. Rev. B: Condens. Matter Mater. Phys.* **2006**, *73*, 035407.
(47) Visnovsky, S.; Lopusnik, R.; Bauer, M.; Bok, J.; Fassbender, J.; Hillebrands, B. Magnetooptic Ellipsometry in Multilayers at Arbitrary Magnetization. *Opt. Express* **2001**, *9*, 121−135.
(48) Gomi, M.; Furuyama, H.; Abe, M. Strong Magneto-optical Enhancement in Highly Ce-Substituted Iron Garnet Films Prepared by Sputtering. *J. Appl. Phys.* **1991**, *70*, 7065−7067.
(49) Goto, T.; Onbaşlı, M. C.; Ross, C. A. Magneto-optical Properties of Cerium Substituted Yttrium Iron Garnet Films with Reduced Thermal Budget for Monolithic Photonic Integrated Circuits. *Opt. Express* **2012**, *20*, 28507−28517.
(50) Savasta, S.; Saija, R.; Ridolfo, A.; Di Stefano, O.; Denti, P.; Borghese, F. Nanopolaritons: Vacuum Rabi Splitting with a Single Quantum Dot in the Center of a Dimer Nanoantenna. *ACS Nano* **2010**, *4*, 6369−6376.
(51) Grotewohl, H.; Deutsch, M. Tunable Geometric Fano Resonances in a Metal/Insulator Stack. *J. Opt.* **2015**, *17*, 085003.
(52) Refki, S.; Hayashi, S.; Rahmouni, A.; Nesterenko, D. V.; Sekkat, Z. Anticrossing Behavior of Surface Plasmon Polariton Dispersions in Metal-Insulator-Metal Structures. *Plasmonics* **2016**, *11*, 433−440.
(53) Song, L.; Wang, Z.; Zhou, D.; Nand, A.; Li, S.; Guo, B.; Wang, Y.; Cheng, Z.; Zhou, W.; Zheng, Z.; Zhu, J. Waveguide Coupled Surface Plasmon Resonance Imaging Measurement and High-throughput Analysis of Bio-interaction. *Sens. Actuators, B* **2013**, *181*, 652−660.
(54) Ekgasit, S.; Thammacharoen, C.; Yu, F.; Knoll, W. Influence of the Metal Film Thickness on the Sensitivity of Surface Plasmon Resonance Biosensors. *Appl. Spectrosc.* **2005**, *59*, 661−667.
(55) Qi, J.; Zeng, J.; Zhao, F.; Lin, S. H.; Raja, B.; Strych, U.; Willson, R. C.; Shih, W. C. Label-Free, in situ SERS Monitoring of Individual DNA Hybridization in Microfluidics. *Nanoscale* **2014**, *6*, 8521−8526.
(56) Zelada-Guillén, G. A.; Sebastián-Avila, J. L.; Blondeau, P.; Riu, J.; Rius, F. X. Label-free Detection of Staphylococcus Aureus in Skin Using Real-Time Potentiometric Biosensors Based on Carbon Nanotubes and Aptamers. *Biosens. Bioelectron.* **2012**, *31*, 226−232.
(57) Tang, Y.; Mernaugh, R.; Zeng, X. Nonregeneration Protocol for Surface Plasmon Resonance: Study of High-Affinity Interaction with High-Density Biosensors. *Anal. Chem.* **2006**, *78*, 1841−1848.
(58) Luk'yanchuk, B.; Zheludev, N. I.; Maier, S. A.; Halas, N. J.; Nordlander, P.; Giessen, H.; Chong, C. T. The Fano Resonance in Plasmonic Nanostructures and Metamaterials. *Nat. Mater.* **2010**, *9*, 707−715.
(59) Nicolas, R.; Lévêque, G.; Marae-Djouda, J.; Montay, G.; Madi, Y.; Plain, J.; Herro, Z.; Kazan, M.; Adam, P. M.; Maurer, T. Plasmonic Mode Interferences and Fano Resonances in Metal-Insulator-Metal Nanostructured Interface. *Sci. Rep.* **2015**, *5*, 14419.

DOI: 10.1021/acsphotonics.7b00091
ACS Photonics 2017, 4, 1403−1412

(60) Hao, J.; Wang, J.; Liu, X.; Padilla, W. J.; Zhou, L.; Qiu, M. High Performance Optical Absorber Based on a Plasmonic Metamaterial. *Appl. Phys. Lett.* **2010**, *96*, 251104.

DOI: 10.1021/acsphotonics.7b00091
ACS Photonics 2017, 4, 1403−1412